Cryo-Electron Tomography of Highly Deformable and Adherent Solid-Electrolyte Interphase Exoskeleton in Li-Metal Batteries with Ether-Based Electrolyte

Bing Han, Xiangyan Li, Qi Wang, Yucheng Zou, Guiyin Xu, Yifeng Cheng, Zhen Zhang, Yusheng Zhao, Yonghong Deng, Ju Li,* and Meng Gu*

The 3D nanocomposite structure of plated lithium (Li$_{Metal}$) and solid electrolyte interphases (SEI), including a polymer-rich surficial passivation layer (SEI exoskeleton) and inorganic SEI "fossils" buried inside amorphous Li matrix, is resolved using cryogenic transmission electron microscopy. With ether-based DOLDME-LiTFSI electrolyte, LiF and Li$_2$O nanocrystals are formed and embedded in a thin but tough amorphous polymer in the SEI exoskeleton. The fast Li-stripping directions are along $[\bar{1}10]$ or $[12\bar{1}]$, which produces eight exposed {111} planes at halfway charging. Full Li stripping produces completely sagging, empty SEI husks that can sustain large bending and buckling, with the smallest bending radius of curvature observed approaching tens of nanometers without apparent damage. In the 2nd round of Li plating, a thin Li$_{BCC}$ sheet first nucleates at the current collector, extends to the top end of the deflated SEI husk, and then expands its thickness. The apparent zero wetting angle between Li$_{BCC}$ and the SEI interior means that the heterogeneous nucleation energy barrier is zero. Due to its complete-wetting property and chemo-mechanical stability, the SEI largely prevents further reactions between the Li metal and the electrolyte, which explains the superior performance of Li-metal batteries with ether-based electrolytes. However, uneven refilling of the SEI husks results in dendrite protrusions and some new SEI formation during the 2nd plating. A strategy to form bigger SEI capsules during the initial cycle with higher energy density than the following cycles enables further enhanced Coulombic efficiency to above 99%.

1. Introduction

The solid electrolyte interphase (SEI) remains a mystery in Li-ion batteries due to the lack of high-resolution analysis tools to obtain atomic structural and chemical information, and its fragility when contacting air, moisture, or electron beam.[1] Li metal in the body-centered-cubic structure (Li$_{BCC}$) is the ultimate anode with the highest specific capacity ($\approx$3860 mAh g^{-1}) among all anode candidates.[2–6] However, the chemical reactivity between Li$_{BCC}$ and the liquid electrolyte leads to SEI formation and the loss or contamination of the precious liquid electrolyte in the cell. Dendrite growth is another concern, which may lead to short-circuiting and catastrophic failure of the battery.

The morphology and crystallinity of the plated Li$_{Metal}$ correlate with electrochemical reversibility of the rechargeable Li-metal batteries (LMB).[7] The literature shows that electrolytes and additives combinations can tune the morphology of the plated lithium (Li$_{Metal}$) and suppress dendrite growth.[3,8,9] Cryogenic transmission electron microscopy (Cryo-TEM) with

B. Han, X. Li, Q. Wang, Y. Zou, Y. Cheng, Z. Zhang, Y. Deng, M. Gu
Department of Materials Science and Engineering
Southern University of Science and Technology
Shenzhen 518055, China
E-mail: gum@sustech.edu.cn
B. Han
Department of Nano Engineering
University of California San Diego
La Jolla, CA 92093, USA
X. Li, Y. Cheng
Academy for Advanced Interdisciplinary Studies
Southern University of Science and Technology
Shenzhen 518055, China

G. Xu, J. Li
Department of Nuclear Science and Engineering
and Department of Materials Science and Engineering
Massachusetts Institute of Technology
Cambridge, MA 02139, USA
E-mail: liju@mit.edu
Y. Zhao, M. Gu
Guangdong-HongKong-Macao Joint Laboratory
for Photonic-Thermal-Electrical Energy
Materials and Devices
Southern University of Science and Technology
Shenzhen 518055, China

direct electron detection cameras can cool down the sample to ≈−193 °C, which allows us to probe the fine details of Li_{Metal} and SEI at the atomic scale.[10–20] The reductive decomposition of electrolyte was believed to result in surficial passivation layer (SEI exoskeleton) on the anode.[21–23] Here, we observe that some components of the SEI exoskeleton can be found on the surface of plated inner crystalline Li_{BCC} as well. Carbon, fluorine, nitrogen, and oxygen atomic impurities are also found within amorphous Li matrix (Li_{Amor}), even turning some near-surface regions into Li_{Amor} instead of Li_{BCC}.

Previously, it was not known to what extent the SEI exoskeleton can adhere to Li_{Metal} and can sustain mechanical deformation. In this work, through cryogenic electron tomography, we show that the SEI exoskeleton can sustain an extraordinary amount of bending and buckling during lithium stripping, resulting in severely sagging, empty husks like a crushed soda can, with the smallest observable bending radius of curvature approaching tens of nanometers without apparent mechanical damage. Essentially, two layers of SEI can be completely folded in contact like a bilayer edge[24] in paper-folding. Upon re-lithiation, the crushed exoskeletal SEI shell can be refilled and expands outward, with initially a sheet-like Li_{Metal} that indicates complete wetting (Young's contact angle θ=0) and thus zero heterogeneous nucleation energy barrier and zero local overpotential contribution from the nucleation event. However, when the volumetric capacity of the old SEI sac is finally exceeded, it may fracture and some SEI fragments may be buried beneath the overgrowing Li_{Metal}, which gradually turns into more inorganic, brittle, "fossil"-like fragments. The exoskeletal SEI forms an empty and deflated 3D SEI network after Li stripping again, and allows newly plated Li_{Metal} to wet and fill its empty spaces, preventing further consumption of Li^+ and electrolyte by isolating the electrolyte from directly touching Li_{Metal}. The formation of an adherent, tough, bendable, and chemically stable 3D SEI exoskeleton in ether-based electrolytes can dramatically increase the coulombic efficiency (CE) in the next cycle. The 3D SEI network inspires us to design such artificial SEI exoskeleton superstructures (e.g., 3D cellular networks) to increase the cycling stability and capacity of batteries.

2. Results and Discussion

The first round of Li_{Metal} plating is conducted using the constant-current mode to a total capacity of 0.5 mAh cm^{-2}. As shown in **Figure 1**, the electroplating in ether-based 1,3-dioxolane/1,2-dimethoxyethane (DOLDME)-lithium bis-trifluoromethanesulfonylimide (LiTFSI) electrolyte (1.0 M LiTFSI salt in 1:1 v/v DOL/DME, with 1% LiNO$_3$ additive) induces the formation of spherical Li_{Metal} particles. Electron diffraction finds the major diffractions of single-crystalline Li_{BCC} spots along [131]$_{BCC}$ zone and diffraction rings of Li$_2$O (111). The magnified cryo-TEM images in Figure 1B,C illustrate the dark SEI exoskeleton and light-contrast Li_{Metal}. There are clearly dark contours, which may result from the diffraction contrast of crystalline Li_{Metal} inside the SEI. Noticeably, a narrow transition zone (≈20 nm thickness) seems to exist from the SEI exoskeleton to the inner crystalline Li_{BCC}, where amorphous Li matrix (Li_{Amor}) is mixed with some nanocrystalline Li$_2$O,

LiF, and possibly other amorphous SEI fragments as shown in Figure 1F. The cryogenic high-resolution transmission electron miscroscopy (Cryo-HRTEM) images of the SEI exoskeleton in Figure 1D,E map out the major inorganic components (Li$_2$O, Li$_2$CO$_3$) inside an organic polymer matrix with the corresponding fast Fourier transform (FFT) displayed in Figure S1, Supporting Information. We believe that the doped impurities of oxygen (O), fluorine (F), nitrogen (N), and carbon (C) in the Li metal come from electrolyte-decomposition side reactions when the electroplating half-cell reaction happens: e$^-$(Metal) + Li$^+$(SEI) = Li atom in Li_{Metal}, leading to the amorphization of Li_{Metal} close to the SEI exoskeleton. Without such atomic impurities, judging from the low melting point of Li_{BCC}, Li atoms in Li_{Metal} should quickly diffuse and coarsen into large crystalline grains instead of becoming Li_{Amor}.[4] Some Li atoms may gradually diffuse into the inner Li_{BCC} region, but leaving the O, F, C, and N atoms enriched in the near-surface region to maintain the amorphous structure. The simultaneous Li plating and reduction of the electrolytes lead to the doping of electrolyte elements into the plated Li matrix. The transition zone between the SEI and Li_{BCC} is the amorphous Li_{Amor} containing C, N, F, and O impurities. This correlates well with the finding of Li$_2$O and LiF in the amorphous amorphous Li_{Amor} transition zone in Figure 1F. In addition, the polymer component in the SEI exoskeleton may partially decompose to amorphous carbon species (likely LiC$_x$) and Li$_2$O when contacting Li metal, which explains the origin of the transition zone. The cryogenic electron energy loss spectroscopy (cryo-EELS) analysis in Figure 1G–I shows the content of Li, C, N, O, F in the empty SEI husks. The identification of F K and O K edges are in good agreement with the previously identified Li$_2$O and LiF nanocrystalline regions using cryo-HRTEM in Figure 1E,F. The nitrogen and carbon may form amorphous components coexisting inside Li_{Amor}. In Figure 1G, the Li K edge shows a blunt plateau feature, which comes from the mixed valent states of Li in the SEI (such as LiC$_x$, Li$_2$O, LiF, Li (polymer), etc.). The C K EELS fine structure in Figure 1H shows similar features compared with amorphous carbon[25] or polyimide,[26] which is consistent with the amorphous nature of the polymeric matrix of the SEI.[11,27] The sharp C K peak at 285 eV originates from the transition of C 1s orbital to the π^*(C=C) orbital.[26] The second blunt peak of the C K edge corresponds to the σ^*(C−N, C−O, C−C) bonding inside the empty SEI husks.[26] We also detect a clear N K, O K, and F K edge in the empty SEI husks in Figure 3I, which confirms the content of such elements in the SEI. These N and F dopants likely come from the LiTFSI (CF$_3$SO$_2$NLiSO$_2$CF) salts in our DOLDME electrolyte with 1% LiNO$_3$.

The SEI exoskeleton acts as the protection layer for the plated Li-metal electrode, preventing the further reaction with the electrolyte due to its electron and molecular impermeabilities (but still conductive to Li$^+$). We probed the morphology of the SEI after half-way stripping (charged to 0.25 mAh cm^{-2}) of Li metal in **Figure 2**A,B. The plated solid Li particles shrank, and the SEI exoskeleton began to fold and wrinkle as shown clearly by the cryogenic scanning transmission electron miscroscopy (Cryo-STEM) tomography in Figure 2A. Judging from the morphology of the central Li core, the Li$^+$ escapes from all surface areas but at different rates. The Cryo-STEM tomography tilt series in Figure 2A show eight surface planes labeled with

**ADVANCED
SCIENCE NEWS**

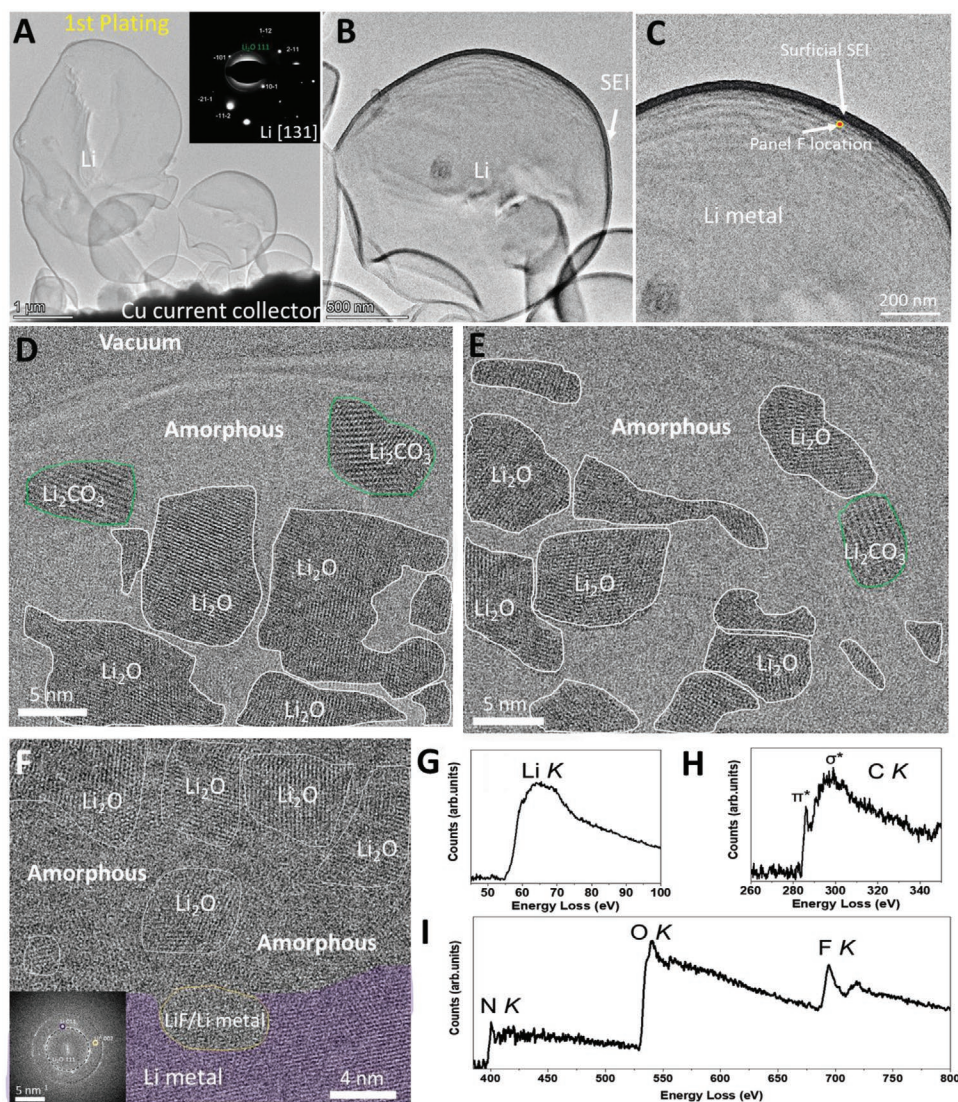www.advancedsciencenews.com

**ADVANCED
MATERIALS**

www.advmat.de

Figure 1. Li dendrite and SEI formed using DOLDME with LiTFSI additive. A,B) Low-magnification Cryo-TEM showing Li metal and SEI. C) Magnified Cryo-TEM showing the clear dark fringes of the impurity gradient from surface to inner bulk; the region in between the yellow line and SEI exoskeleton is the transition zone. D,E) Cryo-HRTEM phase map of different components in the surficial SEI. F) Cryo-HRTEM and FFT of the skeleton SEI showing the LiF and Li_2O inside the amorphous Li matrix just underneath the surficial SEI. G) Li K edge, H) C K edge, and I) N K, O K, and F K edges obtained at the SEI.

"P1–P8" at halfway stripping. Detailed electron diffraction analysis (Figure 2B–D) and Wulff reconstruction (Figure 2E–G) show that the eight exposed surfaces are {111} planes with a ≈71° angle (Figure 2A,F) between the adjacent facets. For best viewing, Figure S2, Supporting Information, displays the reconstructed 3D tomography of the half-way stripped Li particle viewed from different angles (see also Movies S2 and S3, Supporting Information, for rotational and cross-sectional slicing details). The atomic model in Figure 2E matches well with the experimental image in Figure 2B, confirming the exposed faces to be {111} plane of Li_{BCC}. Therefore, the cupped morphology of the halfway stripped Li particles is induced by the preferred {111} stripping planes. The fast-stripping directions should be the perpendicular directions of {111} planes, such as [$\bar{1}$10], [12$\bar{1}$], or other crystallographic directions. In addition, we noted that the SEI exoskeleton remains wrapped around the shrunken

Li_{Metal} particle during the stripping process in Figure 2A,B. This tight wrapping behavior of SEI/Li_{Metal} facilitates the Li stripping by reducing the transport path length of Li^+, ensuring that the Li^+ goes out directly across the SEI skin without much internal diffusion on the surfaces of Li_{Metal}. This can only mechanically happen if the SEI exoskeleton has strong adhesion energy with Li_{Metal}, and is also thin and flexible (a shell's bending stiffness is $Eh^3/12$, where E is the Young's modulus and h is its thickness), and tough, otherwise it would either detach from the Li_{Metal} or fracture, both of which are deleterious to the Li_{Metal} cycling kinetics.

The fully charged sample (charged to 0.5 mAh cm^{-2}) in **Figure 3**A,B shows totally deflated and empty SEI husks after full stripping of Li_{Metal}. The SEI husks shrink, fold but do not fragment or collapse after Li stripping, indicating amazing robustness, considering how thin they are. The macro-view of
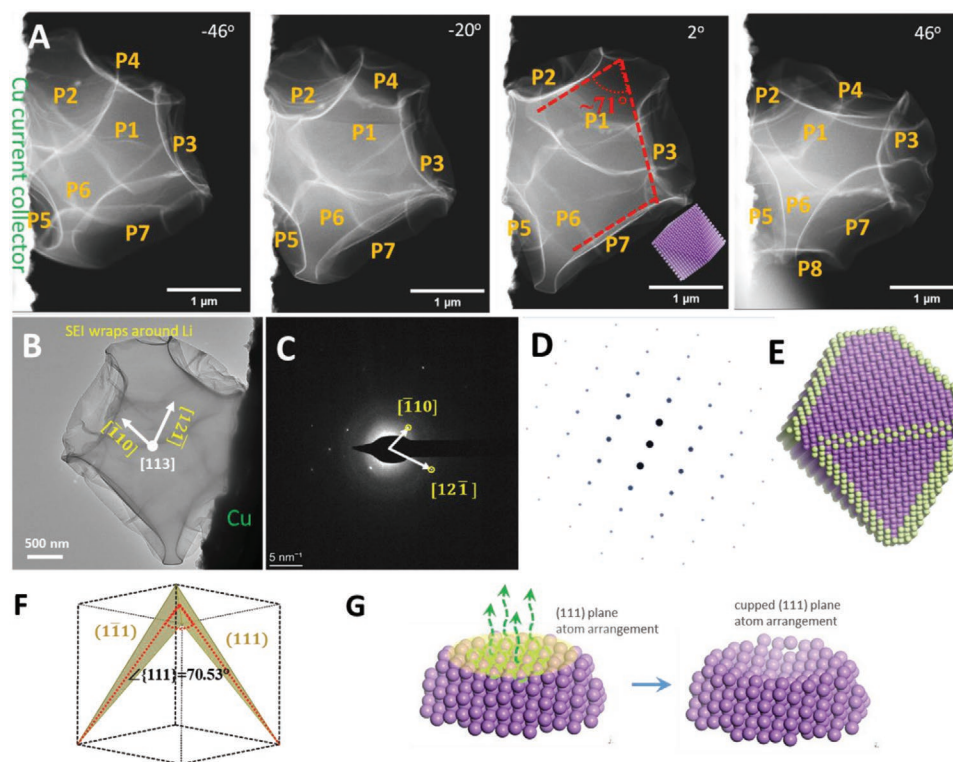
Figure 2. A) Cryo-STEM tomography tilt series viewing of the morphology of a halfway stripped Li particle (charged to 0.25 mAh cm^{-2}). B) TEM image of the halfway stripped Li particle. C) Corresponding [113] zone electron diffraction pattern of the particle in (B). D) Calculated [113] zone diffraction pattern using Crystal Maker software. E) Wulff reconstruction of the halfway stripped Li model. F) Schematic illustrations of relationship between {111} set of planes. G) Atomic model showing the cupped surface induced by atom stripping along the (111) plane.

the empty deflated SEI husks after Li stripping cycle is exemplified in Figure S3, Supporting Information, confirming that the vast majority of the SEI husks are completely empty. The Cryo-STEM tilt series in Figure 3C (see also Movie S4, Supporting Information) illustrate the deflated balloon morphology of an SEI husk at different viewing angles. The geometry (only ≈40 nm thick as labeled by the yellow arrow) indicates that the two-sided SEI exoskeleton can fold to form intimately contacting bilayers after stripping out the Li metal. The white arrows in the Cryo-STEM images acquired at −26° and 8° tilt angles in Figure 3C points out the remaining tiny piece of Li$_{Metal}$ yolk in the center of the empty SEI husk. This provides strong evidence that the central Li$_{Metal}$ yolk gets out of the SEI at last, and whatever is left unstrippable is due to loss of electronic percolation path to the current collector. Therefore, this little piece of Li metal is the inactive "dead Li". Figure 3D displays the 3D tomographic view of the deflated husks from different angles, where the SEI layers shrank to fold intimately together to form a double-folded SEI feature with the total thickness of only ≈40 nm (see also Movies S5 & S6, Supporting Information, for rotational and cross-sectional slicing views). The Cryo-STEM imaging and Cryo-EELS maps in Figure S4, Supporting Information, confirm the presence and distribution of Li, C, N, O, F at the empty SEI. The strong bonding and flexibility of the amorphous and polymeric SEI matrix act to maintain the structural integrity of SEI exoskeleton during repeated volume changes upon Li stripping and plating. The SEI husks shrank and fold, but did not shatter. We also probed the morphology

evolutions of the Li deposit and SEI from the ether-based electrolyte using scanning electron microscopy (SEM) analysis in Figure S5, Supporting Information, which shows the same result as concluded based on our Cryo-TEM analysis.

In contrast, in carbonate-based ethylene carbonate (EC)/diethyl carbonate (DEC)-fluoroethylene carbonate (FEC)/LiPF$_6$ electrolyte, the electrochemically deposited Li metal is flake-shaped (as shown by the Cryo-TEM image in Figure S6, Supporting Information, and the SEM images in Figure S7, Supporting Information), and its SEI husks are larger and porous after Li stripping. The tilt series, rotational-3D view, and cross-sectional view of the reconstructed SEI can be found in Figures S8 and S9 and Movies S7 and S9, Supporting Information. The observed pores in the SEI husk in carbonate-based EC:DEC-FEC/LiPF$_6$ electrolyte are rather large (up to ≈1 μm) as shown in Figure S9, Supporting Information, indicating that the central Li-metal yolk decoupled with the SEI layer during the Li stripping cycle. Then, the Li$^+$ ions have to diffuse along the Li-metal surface before reaching the SEI layer, and then transmit through the SEI to the liquid electrolyte. The large pores size and porous nature indicate that the SEI produced in carbonate-based liquid electrolyte has less adherence with Li metal and poorer flexibility than the one formed in ether-based electrolyte. The lower diffusivity on the Li-metal surface (than in liquid electrolyte) and longer diffusion path increases the possibility of non-uniform local Li-metal stripping and chances of forming inactive "dead Li". In sharp comparison, the central Li metal maintains intimate contact with

**ADVANCED
SCIENCE NEWS**

www.advancedsciencenews.com
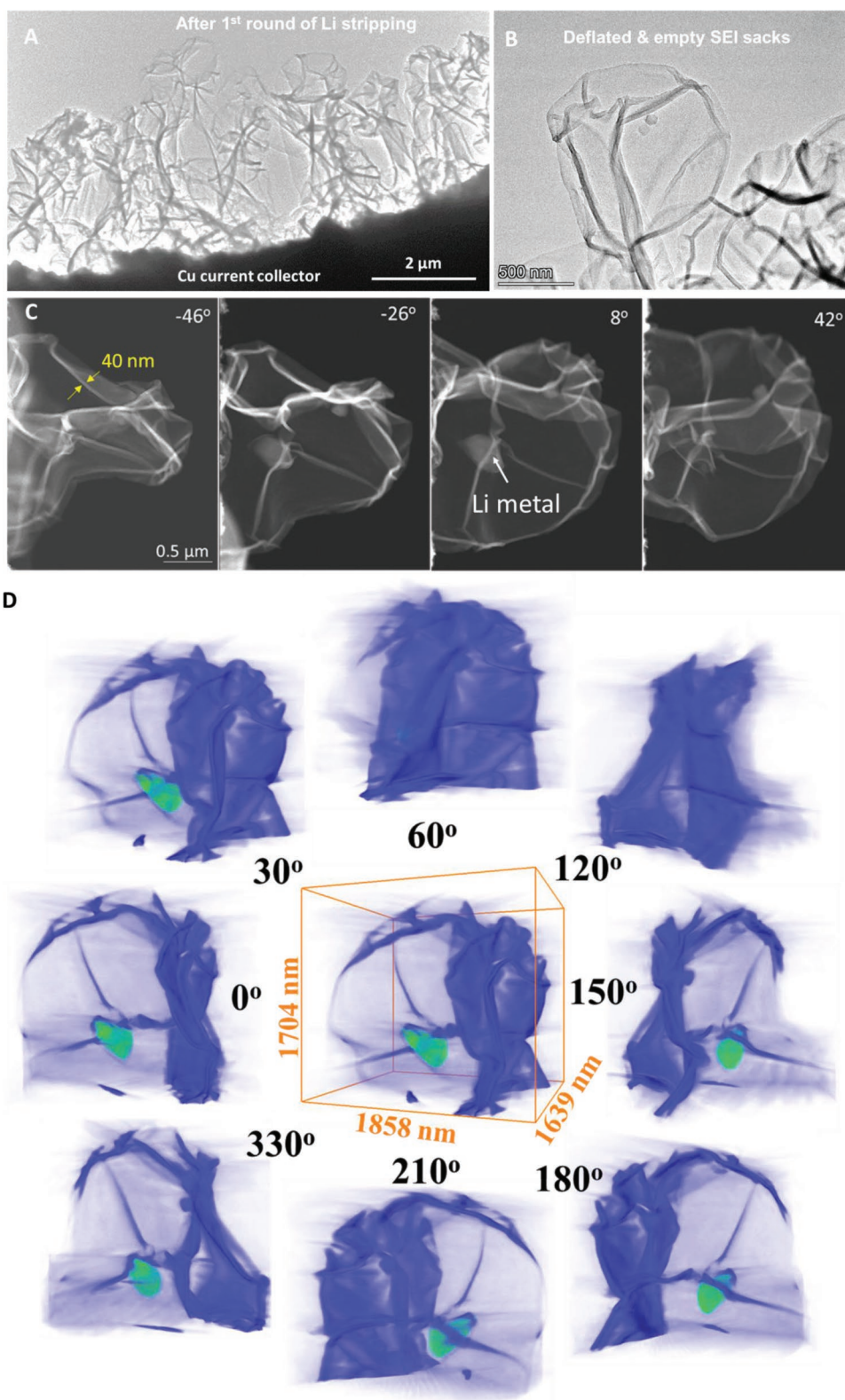
**ADVANCED
MATERIALS**

www.advmat.de

Figure 3. A,B) Cryo-TEM of the remaining empty husks after full stripping of Li. C) Cryo-STEM tomography tilt series viewing of the deflated empty SEI husk at different angles;(see also Movie S3, Supporting Information). D) 3D reconstruction of the SEI husk and central Li yolk (highlighted in green) after Li stripping in DOLDME-LiTFSI with 1% $LiNO_3$ (see also Movies S4–S6, Supporting Information, to view the deflated SEI husk at different angles).

**ADVANCED
SCIENCE NEWS**

www.advancedsciencenews.com

**ADVANCED
MATERIALS**

www.advmat.de

the shrinking SEI during Li stripping in ether-based electrolyte, where the Li$^+$ can diffuse through the contacting SEI to go directly into the electrolyte with high ion diffusion efficiency. As observed, the cycling CE in carbonate-based EC/DEC-FEC electrolyte decays quickly from 95 to 80% after 80 cycles, while the cell cycling with ether-based DOLDME-LiTFSI electrolyte retain stable and high CE of ≈97.5% or higher in most cycles in Figure S10, Supporting Information. The solvent, salt, and additives of the liquid electrolyte are likely to play very important roles in defining the mechanical strength and flexibility of the SEI.

Upon reversal of the voltage bias, the empty SEI husks forming the 3D Li$^+$-conductive solid electrolyte network are ready to be filled by newly plated Li$_{Metal}$, so heretofore we analyzed the morphology after the second round of Li plating. As shown in **Figure 4**A–F, after Li plating up to 0.1 mAh cm^{-2} capacity, the deflated husks start to be filled by Li$_{Metal}$. First, a thin layer of Li$_{Metal}$ nucleates at the bottom of the SEI husk in contact with the Cu current collector. This jacks up a 2D adhesion crack that separates the previously intimately adherent SEI bilayer. Then, the Li atoms diffuse up along the SEI skin. The Cryo-HRTEM in Figure 4B shows the clear Li$_{BCC}$ $\{10\bar{1}\}$ set of planes from the
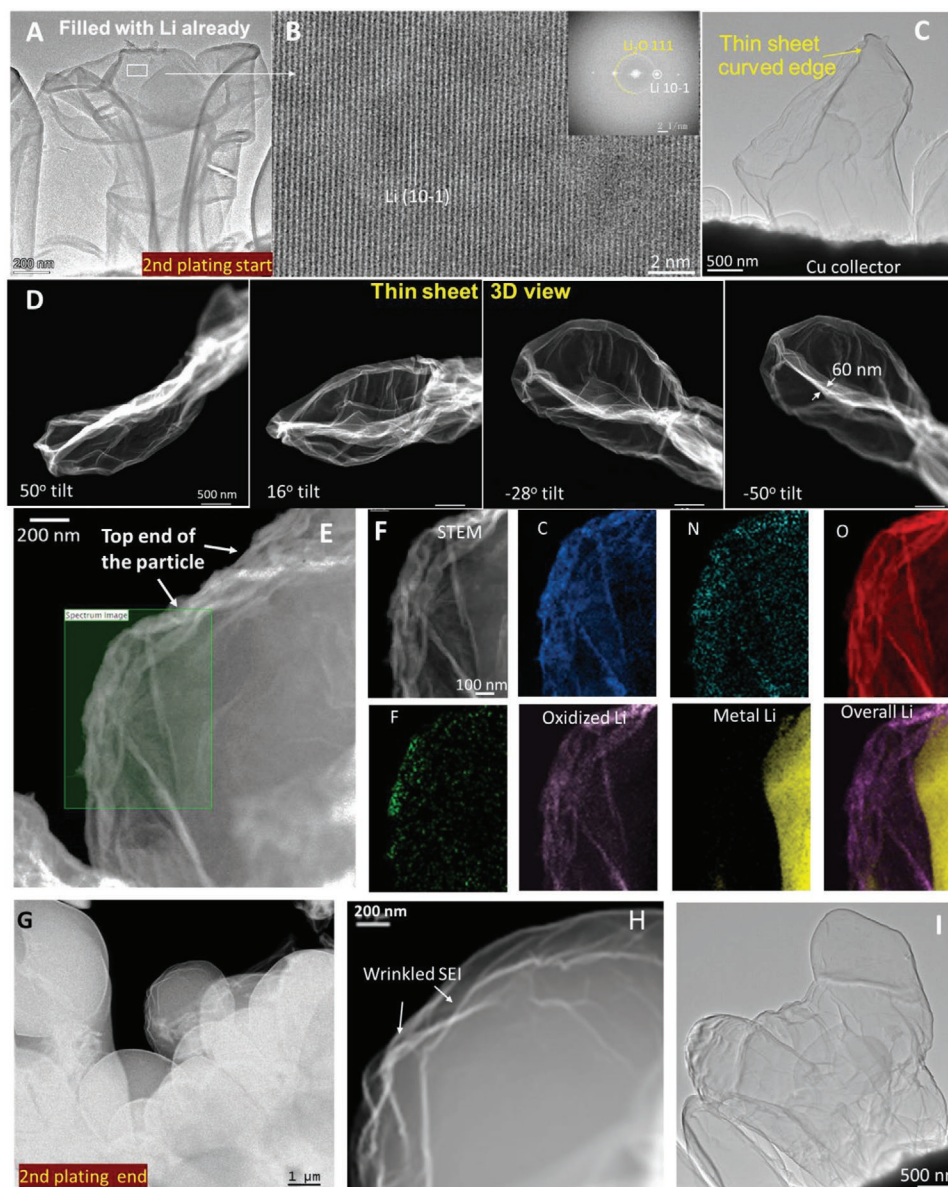

Figure 4. Li particles and SEI at 2nd round of plating up to 0.1 mAh cm^{-2} energy capacity. A) Low-magnification Cryo-TEM of the SEI filled with thin layer of Li. B) Cryo-HRTEM of the rectangle region in (A) showing the Li$_{BCC}$ lattice and corresponding FFT as the inset. C) SEI with curved edge showing the thin Li sheet in it. D) Cryo-STEM tomography tilt series revealing the Li thin sheet morphology at the 2nd round of plating into the SEI (see also Movies S10–S12, Supporting Information, for the tilt series and reconstructed tomography views). E) STEM and F) EELS map of C, N, O, F, oxidized Li, metallic Li deconvoluted from the Li K edge and overall Li map after charging to 0.1 mAh cm^{-2} energy capacity. G,H) Cryo-STEM and I) Cryo-TEM images of the Li particles after full 2nd round of Li plating to 0.5 mAh cm^{-2}.

rectangular region in Figure 4A, confirming Li diffusion up to the very top of the SEI husk, even when the SEI husk remains largely deflated. The curved edges in Figure 4C also show the formation of very thin sheets of Li_{Metal} inside the deflated SEI husk, which means that the Li atoms get sucked up to fill the whole SEI husk once nucleated at the bottom, and extends the 2D adhesion crack mainly in the two in-plane directions. Furthermore, we used Cryo-STEM tomography to see the thin sheet morphology in 3D in Figure 4D (see also Figures S11 and Movies S10 and S12, Supporting Information), in which the tilt series images at different viewing angles illustrate the Li_{Metal} thin sheet morphology at this initial plating stage. The thickness of the folded SEI plus the Li_{Metal} thin sheet inside is only 60 nm. Therefore, the Li_{Metal} sheet itself is merely a few nanometers in thickness, while microns in extent, qualifying as a "2D material". In addition, we use the STEM EELS to probe the growth of the Li_{Metal} thin sheet in the SEI in Figure 4E,F. From the EELS mapping, we identify that the SEI contains C, N, O, F, and Li signals. Using EELS multiple linear least square fitting, we deconvolute the metallic Li and oxidized Li from the Li K edge, and clearly differentiate the metallic Li inside the deflated SEI husk. The Li_{Metal} is only a few hundred nanometers away from the wrinkled SEI edges, indicating Li_{Metal} sheet growing to the very top end even at the initial plating stage. This striking 2D growth behavior of Li_{Metal} thin sheet in the empty SEI husks reflects perfect wetting between Li_{Metal} and SEI,[27] that is to say, the equilibrium wetting

angle θ between Li_{Metal} and SEI should be zero. In the case of perfect wetting $\theta = 0$, theory predicts that a few-monolayer thick precursor thin film would spread, which has been modeled by de Gennes et al.[28–30] The area with the shortest Li^+ diffusion length across the SEI gets filled by Li first, since electronic conductivity in Li_{Metal} is much higher than the Li^+ diffusivity across SEI. The deflated SEI husks show intimately contacting SEI from both sides. The shortest Li^+ diffusion path is crossing only the SEI skin from the electrolyte. Therefore, once a thin layer of Li metal nucleates at the bottom, the electrons can be conducted up to facilitate the following growth of the Li_{Metal} thin sheets. After the perfectly wetting Li_{BCC} precursor film has spread to the end of the husk, with further plating the SEI husk will grow fatter in volume. After fully plating to 0.5 mAh cm^{-2}, most of the SEI husks are then inflated, as shown by the Cryo-STEM and TEM in Figure 4F–H. Figure 4F,G shows the wrinkled SEI exoskeleton surrounding the newly filled Li_{Metal} core, confirming that Li can repeatedly use the leftover SEI exoskeleton. Figure 4H shows fully blown SEI husks after the 2nd round of Li_{Metal} filling.

In addition, as shown by **Figure 5**A, a portion of the SEI husks may get over-filled during the 2nd plating by intaking more Li into its SEI balloon than the 1st plating, inducing the formation of dendrite protrusion and newly formed SEI. These plating behaviors can result in reduced cycling CE, as shown in Figure 5B. We designed a "larger-capsule" strategy, which involves the formation of a bigger SEI capsule during
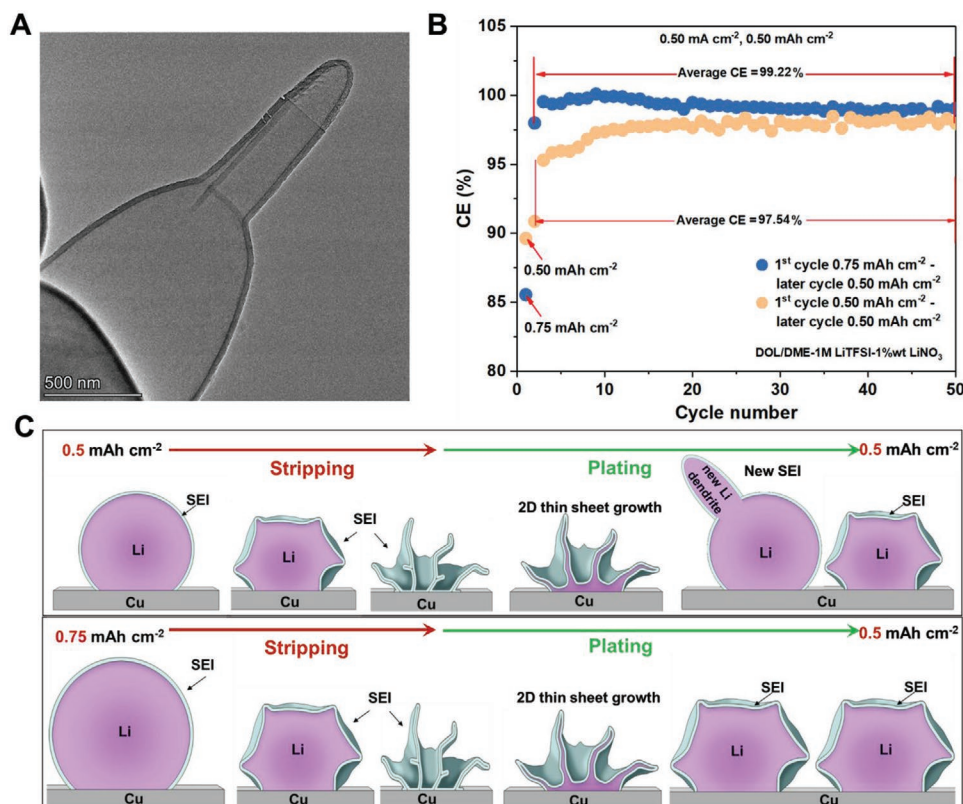

Figure 5. A) Electrochemically deposited Li metal and SEI showing dendrite protrusion after 2nd plating. B) Electrochemical cycling plot showing CE performance enhancement using "larger-capsule" strategy with 0.75 mAh cm^{-2} at the initial Li plating and smaller cycling capacity of ≈0.5 mAh cm^{-2} afterward to avoid dendrite protrusion and additional formation of SEI. C) Schematic drawing showing structural evolution of the electrochemically deposited Li metal and SEI using the traditional cycling compared with the "larger-capsule" strategy.

**ADVANCED
SCIENCE NEWS**
www.advancedsciencenews.com

**ADVANCED
MATERIALS**
www.advmat.de

the initial cycling, which can better endure uneven Li plating in the following cycling in this case. As schematically shown in Figure 5C, after the 1st round of Li plating in liquid electrolyte, the plated spherical Li particles first form a percolating SEI exoskeleton. Then the ensuing Li stripping induces the formation of shrunk Li_{Metal} core tightly wrapped by the SEI skin, which reduces the diffusion path and facilitates the further stripping of Li to the electrolyte. Therefore, the ability to fold and wrap around the Li_{Metal} during stripping is an important characteristic of a good SEI skin. During the Li stripping, the resilient SEI exoskeleton must fold and wrinkle, largely without breaking its structural integrity and liquid tightness. Ether-based DOLDME-LiTFSI with 1% $LiNO_3$ is known for its relatively stable Li-metal anode cycling, and we propose the superior mechanical properties of its SEI with Li_{Metal} is the main reason. The Li stripping finally induce the formation of 3D SEI network with contacting double-layered features like folded paper or deflated balloons, as shown in Figure 5C. The mechanically tough and flexible 3D SEI network allows Li to go in again with voltage reversal, nucleating first at the current collector, then fast diffusing to the top of the SEI husk to form thin-sheet morphology in the 2nd round of Li plating, and then, newly plated Li inflates the SEI husks. However, the 2nd round of plating may produce dendrite protrusions and additional amounts of new SEI due to uneven Li refilling into the SEI balloons, as shown in Figure 5C. Therefore, we designed a "larger-capsule" strategy, which involves simply forming bigger Li-metal particles and SEI husks at the initial cycling with a larger current density of 0.75 mAh cm^{-2}. The as-formed bigger SEI husks can better withstand possible uneven Li refilling without growing protrusions and additional SEI during the following rounds of Li plating at 0.5 mAh cm^{-2}. Therefore, the average cycling CE is ≈99.22% for the "larger-capsule" approach compared to ≈97.54% for the standard approach counting from the 2nd to 50th cycles.

A good liquid electrolyte and additive combination should induce the formation of a continuous SEI exoskeleton with the highly adherent and flexible polymeric matrix that faces the liquid electrolyte, which mediates the transport of Li^+ ions in the following cycles in Figure S12, Supporting Information. Purely inorganic particles like Li_2O stacking together can be easily shattered by the large buckling and bending. Therefore, the resiliency of the polymer backing of the SEI exoskeleton ensures the repeated usage of the SEI during the ensuing cycling.

On the other hand, the inward-facing side of the exoskeletal SEI is clearly highly lithiophilic,[27,31] so much so that the SEI does not have a sharp interface with the Li metal, and the wetting angle θ is zero from our Cryo-TEM observation. This is highly beneficial for the second plating, because according to the heterogeneous nucleation theory,[32] the energy barrier of nucleating Li_{Metal} inside an interface scales as

$$Q_{hetero} = Q_{homo}(2 + \cos\theta)(1 - \cos\theta)^2/2 \qquad (1)$$

where Q_{homo} is the standard homogeneous nucleation barrier. When $\theta \to 0$, $Q_{hetero} \to 0$, thus complete wetting of the double-folded SEI interior with Li_{Metal} means there is zero nucleation overpotential required in the 2nd, 3rd, ... plating (as shown in

Figure S13, Supporting Information), beyond the usual Li^+ and e^- long-range transport losses. This addresses the reason why in the first plating of Li_{Metal}, there is often a significant overpotential signature in the voltage versus capacity curve (as the SEI exoskeleton has not yet formed), but such overpotential signature rapidly drops with subsequent cycling. The top ≈15–20 nm of the SEI is electronically insulating with distinct elemental concentration difference, but the inward-facing transition zone is metallic despite the impurities that often lead to Li_{Amor} (or at least ultra-nanocrystalline or partially amorphous). This transition zone is seen to achieve perfect wetting with Li_{BCC}. Thus, rather than a sharp "layer", the SEI may be better thought of as a gradient structure, with the metal-to-insulator transition as one sweeps from the interior to the SEI exterior.

3. Conclusions

Cryo-TEM and Cryo-STEM tomography allow us to reach a clear atomic-scale picture of the SEI exoskeleton formed in DOLDME-LiTFSI with 1% $LiNO_3$, which is known to be a superior liquid electrolyte for Li_{Metal} cycling. The inorganic components, including nanocrystalline Li_2O, Li_2CO_3, LiF islands, are distributed inside a continuous and resilient polymer matrix, which forms the SEI exoskeleton. The impurities concentration gradient from surface to inside created a transition zone between the SEI exoskeleton and inner Li_{BCC}, via an amorphous lithium matrix (Li_{Amor}) with a higher concentration of O, F, and C. The SEI exoskeleton has strong adhesion and perfect wetting with Li_{Metal} on the inside, and on the outward liquid-facing side, develops a resilient organic polymer backing. Thereupon, shrinkage, bending, and folding of the SEI networks can repeatedly take place in cycling without causing fragmentation or collapse of the SEI network. A multi-cellular 3D SEI network remains intact after the Li stripping process, which allows Li^+ to transport, nucleate, and grow in the following plating cycles. Since the SEI is seen to have zero equilibrium wetting angle with Li_{Metal}, subsequent new Li_{Metal} phase nucleation can occur without any local overpotential. We also proposed a "larger-capsule" strategy, which can better withstand the uneven refilling of SEI husks without growing dendrite protrusions and additional SEIs, further enhancing the CE. Our finding expands the understanding of SEI and reveals a clear picture of the thin but robust and adherent SEI exoskeleton formed with ether-based electrolyte.

Supporting Information

Supporting Information is available from the Wiley Online Library or from the author.

Acknowledgements

Conflict of Interest

The authors declare no conflict of interest.

Author Contributions

B.H. and X.L. contributed equally to this work. M.G. supervised the project. M.G., B.H., and J.L. designed the experiment and wrote the paper; M.G., B.H., and X.L. revised the paper; B.H. and Y.Z. carried out the cryo-TEM and battery testing; M.G., J.L., B.H., and Q.W. analyzed the data; X.L. carried out 3D characterization; all authors discussed the paper.

Data Availability Statement

Research data are not shared.

[1] J. B. Goodenough, Y. Kim, *Chem. Mater.* **2010**, *22*, 587.

[2] L. Suo, W. Xue, M. Gobet, S. G. Greenbaum, C. Wang, Y. Chen, W. Yang, Y. Li, J. Li, *Proc. Natl. Acad. Sci. USA* **2018**, *115*, 1156.

[3] B. Han, D. Xu, S.-S. Chi, D. He, Z. Zhang, L. Du, M. Gu, C. Wang, H. Meng, K. Xu, Z. Zheng, Y. Deng, *Adv. Mater.* **2020**, *32*, 2004793.

[4] Y. Chen, Z. Wang, X. Li, X. Yao, C. Wang, Y. Li, W. Xue, D. Yu, S. Y. Kim, F. Yang, A. Kushima, G. Zhang, H. Huang, N. Wu, Y.-W. Mai, J. B. Goodenough, J. Li, *Nature* **2020**, *578*, 251.

[5] W. Xu, J. Wang, F. Ding, X. Chen, E. Nasybulin, Y. Zhang, J.-G. Zhang, *Energy Environ. Sci.* **2014**, *7*, 513.

[6] J. M. Tarascon, M. Armand, *Nature* **2001**, *414*, 359.

[7] B. L. Mehdi, A. Stevens, J. Qian, C. Park, W. Xu, W. A. Henderson, J.-G. Zhang, K. T. Mueller, N. D. Browning, *Sci. Rep.* **2016**, *6*, 34267.

[8] F. Ding, W. Xu, G. L. Graff, J. Zhang, M. L. Sushko, X. Chen, Y. Shao, M. H. Engelhard, Z. Nie, J. Xiao, X. Liu, P. V. Sushko, J. Liu, J.-G. Zhang, *J. Am. Chem. Soc.* **2013**, *135*, 4450.

[9] H. Ota, K. Shima, M. Ue, J.-i. Yamaki, *Electrochim. Acta* **2004**, *49*, 565.

[10] Y. He, L. Jiang, T. Chen, Y. Xu, H. Jia, R. Yi, D. Xue, M. Song, A. Genc, C. Bouchet-Marquis, L. Pullan, T. Tessner, J. Yoo, X. Li, J.-G. Zhang, S. Zhang, C. Wang, *Nat. Nanotechnol.* **2021**, *16*, 1113.

[11] B. Han, Z. Zhang, Y. Zou, K. Xu, G. Xu, H. Wang, H. Meng, Y. Deng, J. Li, M. Gu, *Adv. Mater.* **2021**, *33*, 2100404.

[12] B. Han, X. Li, S. Bai, Y. Zou, B. Lu, M. Zhang, X. Ma, Z. Chang, Y. S. Meng, M. Gu, *Matter* **2021**, *4*, 3741.

[13] B. Han, Y. Zou, G. Xu, S. Hu, Y. Kang, Y. Qian, J. Wu, X. Ma, J. Yao, T. Li, Z. Zhang, H. Meng, H. Wang, Y. Deng, J. Li, M. Gu, *Energy Environ. Sci.* **2021**, *14*, 4882.

[14] X. Li, B. Han, X. Yang, Z. Deng, Y. Zou, X. Shi, L. Wang, Y. Zhao, S. Wu, M. Gu, *iScience* **2021**, *24*, 103418.

[15] Q. Zhang, B. Han, Y. Zou, S. Shen, M. Li, X. Lu, M. Wang, Z. Guo, J. Yao, Z. Chang, M. Gu, *Adv. Mater.* **2021**, *33*, 2102666.

[16] M. J. Zachman, Z. Tu, S. Choudhury, L. A. Archer, L. F. Kourkoutis, *Nature* **2018**, *560*, 345.

[17] Y. Li, Y. Li, A. Pei, K. Yan, Y. Sun, C.-L. Wu, L.-M. Joubert, R. Chin, A. L. Koh, Y. Yu, J. Perrino, B. Butz, S. Chu, Y. Cui, *Science* **2017**, *358*, 506.

[18] X. Wang, Y. Li, Y. S. Meng, *Joule* **2018**, *2*, 2225.

[19] D. Cheng, T. A. Wynn, X. Wang, S. Wang, M. Zhang, R. Shimizu, S. Bai, H. Nguyen, C. Fang, M.-c. Kim, W. Li, B. Lu, S. J. Kim, Y. S. Meng, *Joule* **2020**, *4*, 2484.

[20] Y. Li, W. Huang, Y. Li, W. Chiu, Y. Cui, *ACS Nano* **2020**, *14*, 9263.

[21] D. Aurbach, M. L. Daroux, P. W. Faguy, E. Yeager, *J. Electrochem. Soc.* **1987**, *134*, 1611.

[22] E. Peled, *J. Electrochem. Soc.* **1979**, *126*, 2047.

[23] E. Peled, D. Golodnitsky, G. Ardel, *J. Electrochem. Soc.* **1997**, *144*, L208.

[24] J. Feng, W. Li, X. Qian, J. Qi, L. Qi, J. Li, *Nanoscale* **2012**, *4*, 4883.

[25] F. Langenhorst, V. L. Solozhenko, *Phys. Chem. Chem. Phys.* **2002**, *4*, 5183.

[26] J. Sedlmair, S.-C. Gleber, C. Peth, K. Mann, J. Niemeyer, J. Thieme, *J. Soils Sediments* **2012**, *12*, 24.

[27] Y. Jin, N.-J. H. Kneusels, L. E. Marbella, E. Castillo-Martínez, P. C. M. M. Magusin, R. S. Weatherup, E. Jónsson, T. Liu, S. Paul, C. P. Grey, *J. Am. Chem. Soc.* **2018**, *140*, 9854.

[28] J. Y. Huang, Y.-C. Lo, J. J. Niu, A. Kushima, X. Qian, L. Zhong, S. X. Mao, J. Li, *Nat. Nanotechnol.* **2013**, *8*, 277.

[29] P. G. de Gennes, *Rev. Mod. Phys.* **1985**, *57*, 827.

[30] F. Brochard-Wyart, P. G. de Gennes, H. Hervert, C. Redon, *Langmuir* **1994**, *10*, 1566.

[31] J. Duan, Y. Zheng, W. Luo, W. Wu, T. Wang, Y. Xie, S. Li, J. Li, Y. Huang, *Natl. Sci. Rev.* **2020**, *7*, 1208.

[32] D. A. Porter, K. E. Easterling, *Phase Transformations in Metals and Alloys*, Chapman & Hall, London, UK **1992**.

ADVANCED MATERIALS

Supporting Information

Cryo-Electron Tomography of Highly Deformable and Adherent Solid-Electrolyte Interphase Exoskeleton in Li-Metal Batteries with Ether-Based Electrolyte

Bing Han, Xiangyan Li, Qi Wang, Yucheng Zou, Guiyin Xu, Yifeng Cheng, Zhen Zhang, Yusheng Zhao, Yonghong Deng, Ju Li,* and Meng Gu*

Supplementary Materials

Cryo-Electron Tomography of Highly Deformable and Adherent Solid-Electrolyte Interphase Exoskeleton in Li-Metal Batteries with Ether-based Electrolyte

Bing Han[1,3#], Xiangyan Li[1,5#], Qi Wang[1], Yucheng Zou[1], Guiyin Xu[2], Yifeng Cheng[1,5], Zhen Zhang[1], Yusheng Zhao[4], Yonghong Deng[1], Ju Li[2,*], Meng Gu[1,4*]

[1]Department of Materials Science and Engineering, Southern University of Science and Technology, Shenzhen 518055, China.

[2]Department of Nuclear Science and Engineering and Department of Materials Science and Engineering, Massachusetts Institute of Technology, Cambridge, MA 02139, USA.

[3]Department of Nano Engineering, University of California San Diego, La Jolla, CA, USA.

[4]Guangdong-HongKong-Macao Joint Laboratory for Photonic-Thermal-Electrical Energy Materials and Devices, Southern University of Science and Technology , Shenzhen 518055, China

[5]Academy for Advanced Interdisciplinary Studies, Southern University of Science and Technology, Shenzhen, 518055, China

[#]These authors contributed equally to this work.

*Correspondence author. gum@sustech.edu.cn (M. Gu); liju@mit.edu (J. Li)

This PDF file includes:

Methods

Supplementary Text

Figures S1 to S9

Other Supplementary Materials for this manuscript include Movies S1 to S9.

Methods

An ether-based electrolyte with 1.0 M lithium bis-trifluoromethanesulfonylimide (LiTFSI) in 1:1 vol/vol 1,3-dioxolane/1,2-dimethoxyethane (DOL/DME) with 1% $LiNO_3$ is used as the electrolyte in our work. The CR2032-type coin cells are assembled in Ar-filled glove box using Li metal as counter and reference electrode. The TEM grid attached on Cu foil is used as the working electrode. The full Li plating and stripping cycles are conducted using constant current mode to a total capacity of 0.5 mAh/cm^2 with a current of 0.5 mA/cm^2. The cycled coin cells are opened in Ar-filled glovebox and the Cu-TEM grid is washed using DMC to remove residue salts or electrolyte, and then instantly frozen in liquid nitrogen and transferred to the cryo-TEM for analysis. The cryo-TEM/STEM/EELS is performed using a Titan Krios with TEM Cs-aberration corrector operating at 300kV. All TEM images are acquired at 77K at low-dose condition (~7 e·Å^{-2}·s^{-1} × 10 s) with a direct detection device camera (Falcon 3) is used to acquire the low-dose TEM images. The STEM images are acquired at 200 e/nm^2; the cryo-EELS are acquired using 11 pA current with 0.1 s dwell time at each pixel for core edges. STEM tomography was applied by imaging samples at different angles. The tilt angle range is listed in Table S1; and the step was 2° in all tilt series. Using Inspect 3D software, the tilt-series were aligned and reconstructed through an expectation maximization algorithm with 25 iterations. The reconstructed 3D images were then colored using Avizo software from Thermo Fisher Scientific.
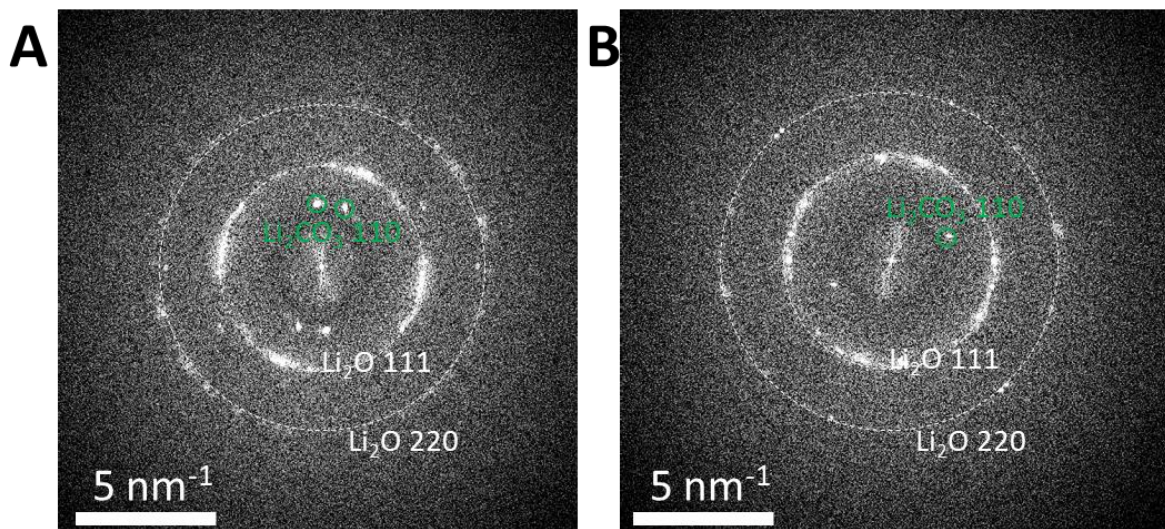
Figure S1. Additional set of FFT diffraction analysis of the high-resolution images corresponding to Figure 1D-E from the sample using DOLDME- LiTFSI with 1% $LiNO_3$. It clearly shows the diffraction signature of Li_2O and Li_2CO_3, which is consistent with the HRTEM analysis in Figure 1.
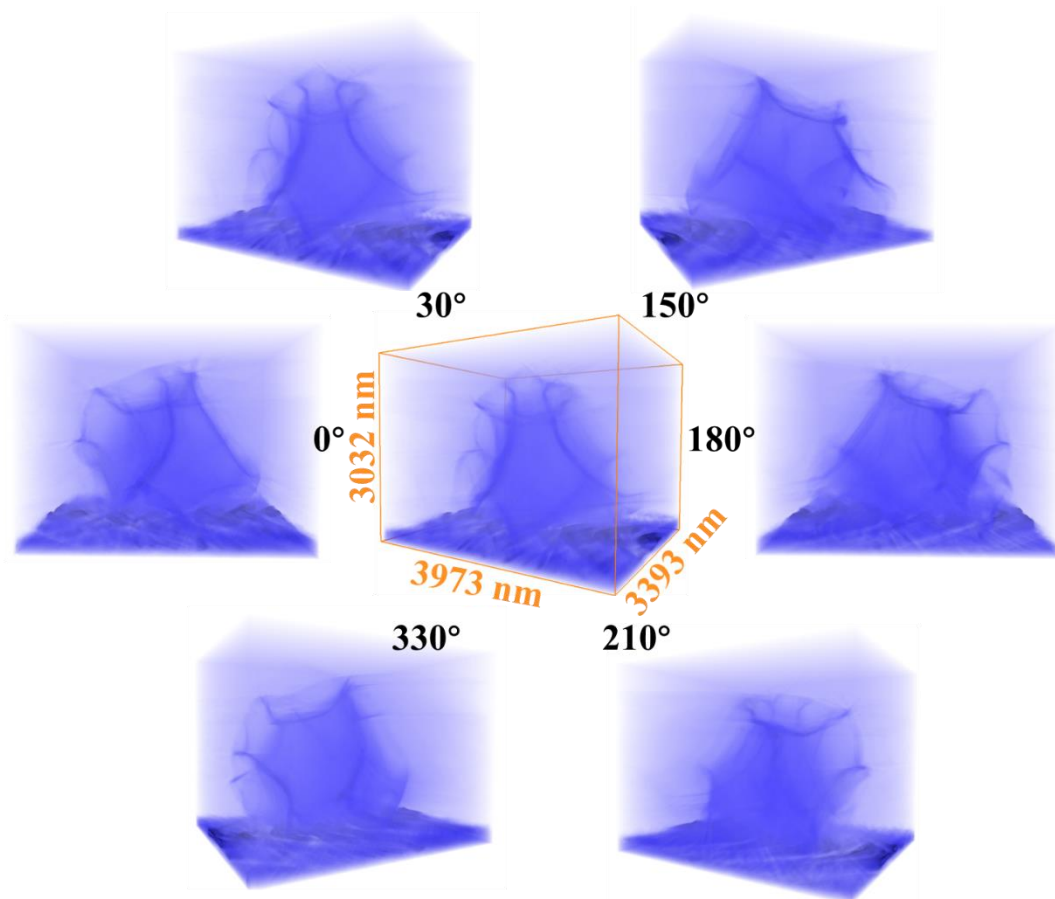
Figure S2. Reconstructed 3D view of the Li particle based on the tilt series in panel A (Please see Movie S1 to view the tilt series and Movie S2&S3 for rotational and cross-sectional tomography of the half-way stripped particle at different angles.)
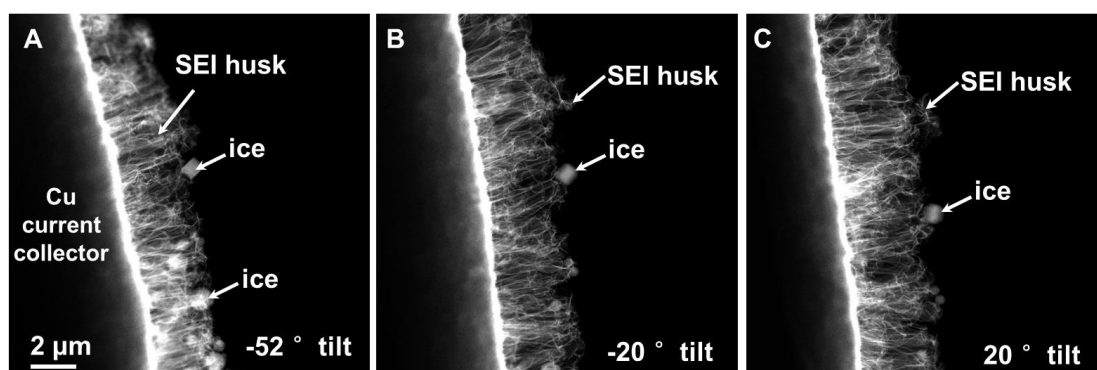
Figure S3 Macro-view of the empty SEI husk after Li stripping, indicating that majority Li metal deposition can be reversibly stripped and the vast majority of the SEI husks are intact and empty after Li stripping.
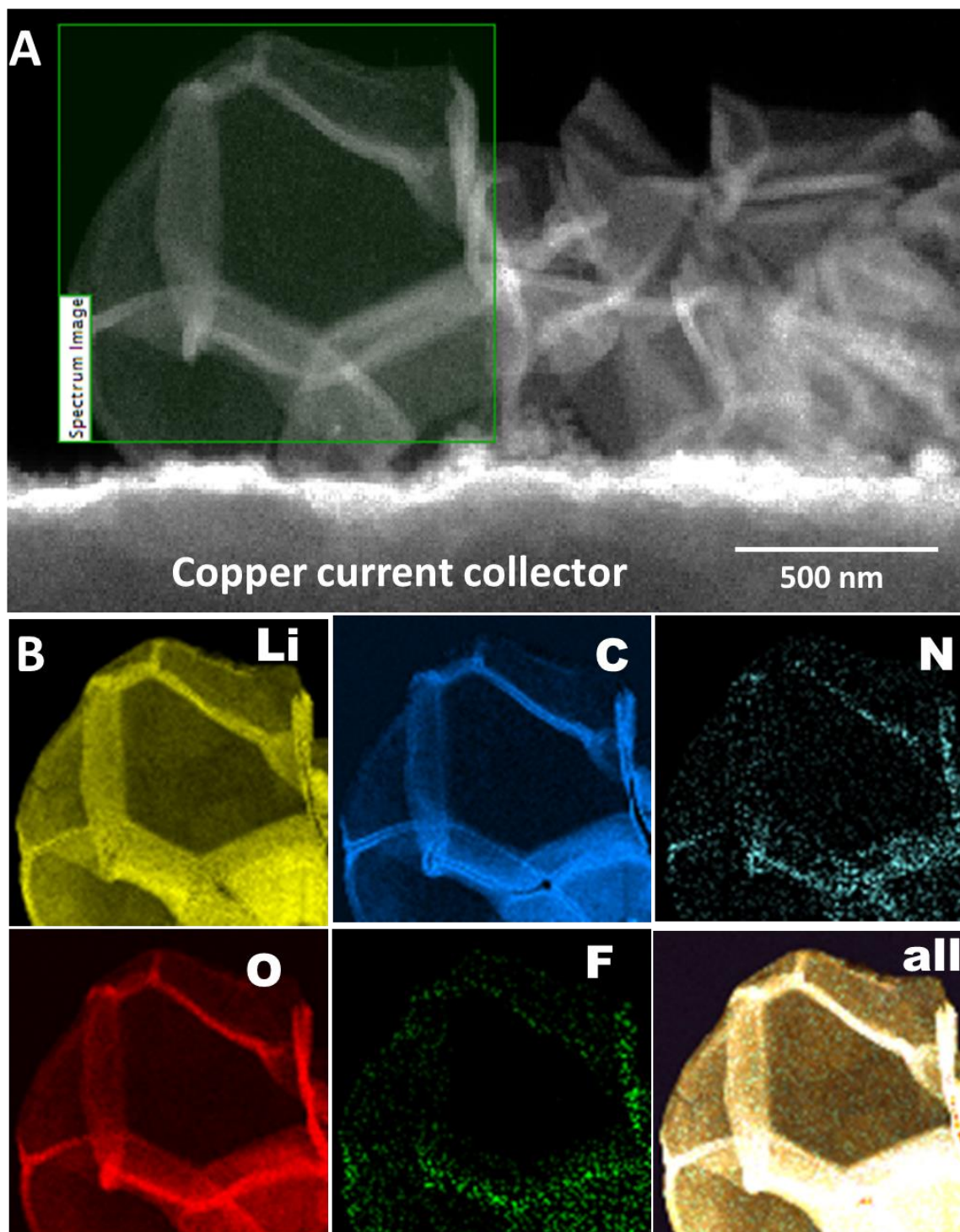
Figure S4. A. cryo-STEM image of the empty and folded SEI husks; B. EELS mapping

showing the content of Li, C, N, O, F in the SEI husks.
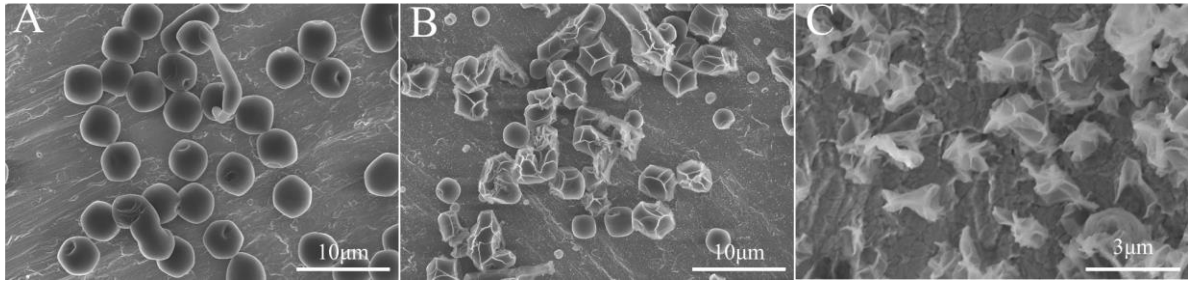
Figure S5. SEM morphology analysis of the sample using DOLDME- LiTFSI with 1% LiNO$_3$. (A) Deposited Li circular particles at the state discharged at 0.5 mA cm^{-2} for 1h; (B) half-way delithiated Li showing faceted surface with SEI folding and shrinking with the inner Li core at half-charged state of 0.5 mA cm^{-2} for 0.5h; (C) morphology of delithiated state charged to 1V showing deflated and folded empty SEI husks.
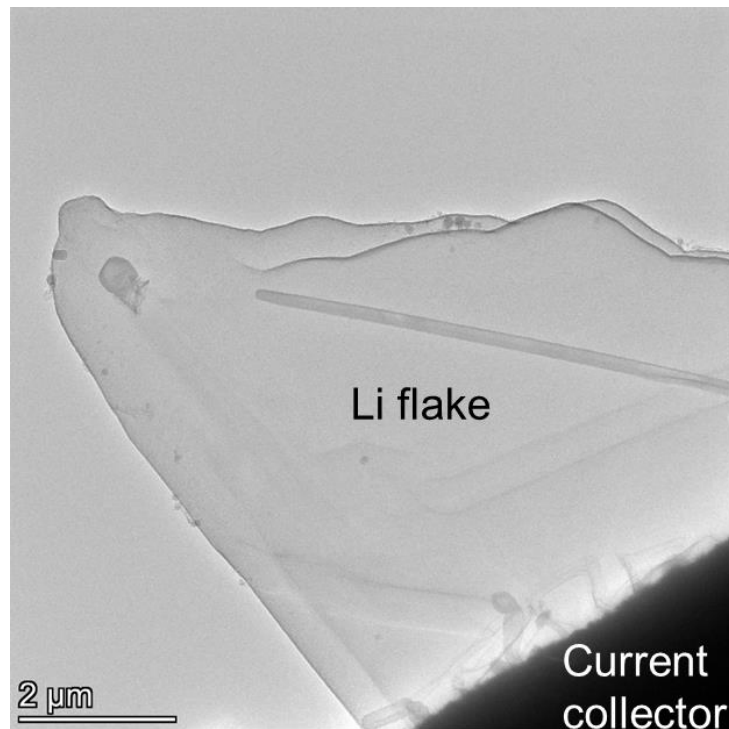
Figure S6 Cryo-TEM image of the electrochemically deposited Li flake in EC:DEC-FEC electrolyte with LiPF$_6$ salt, showing large size up to 8 μm.
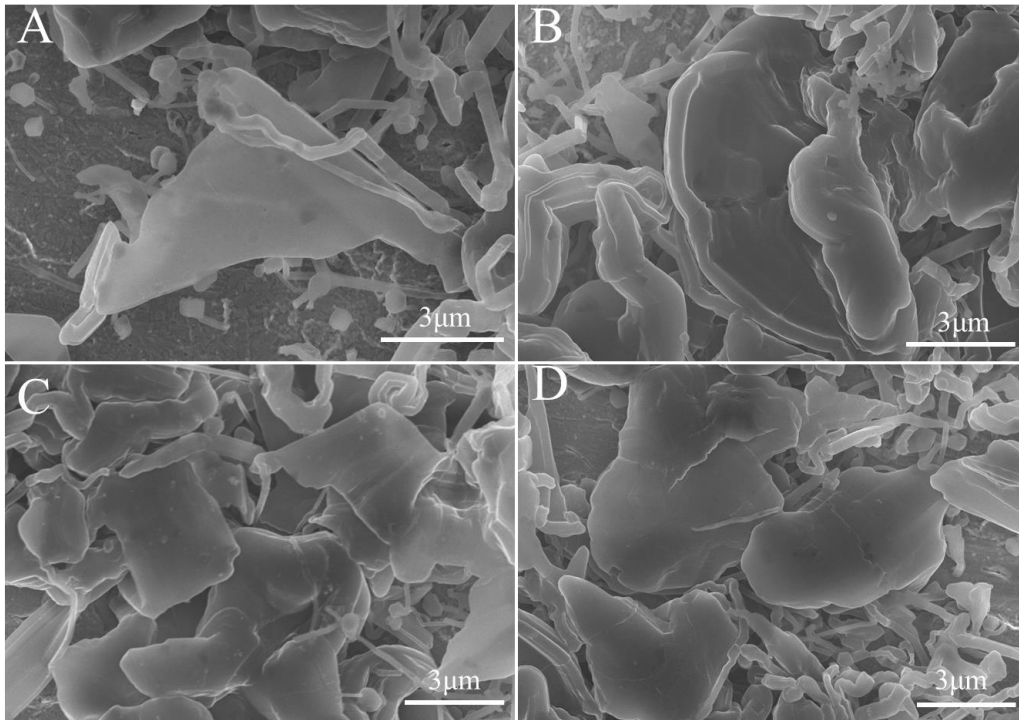
Figure S7. SEM morphology analysis of the deposited Li fakes from EC/DEC-FEC electrolyte by discharging the battery at 0.5 mA cm^{-2} for 1h.
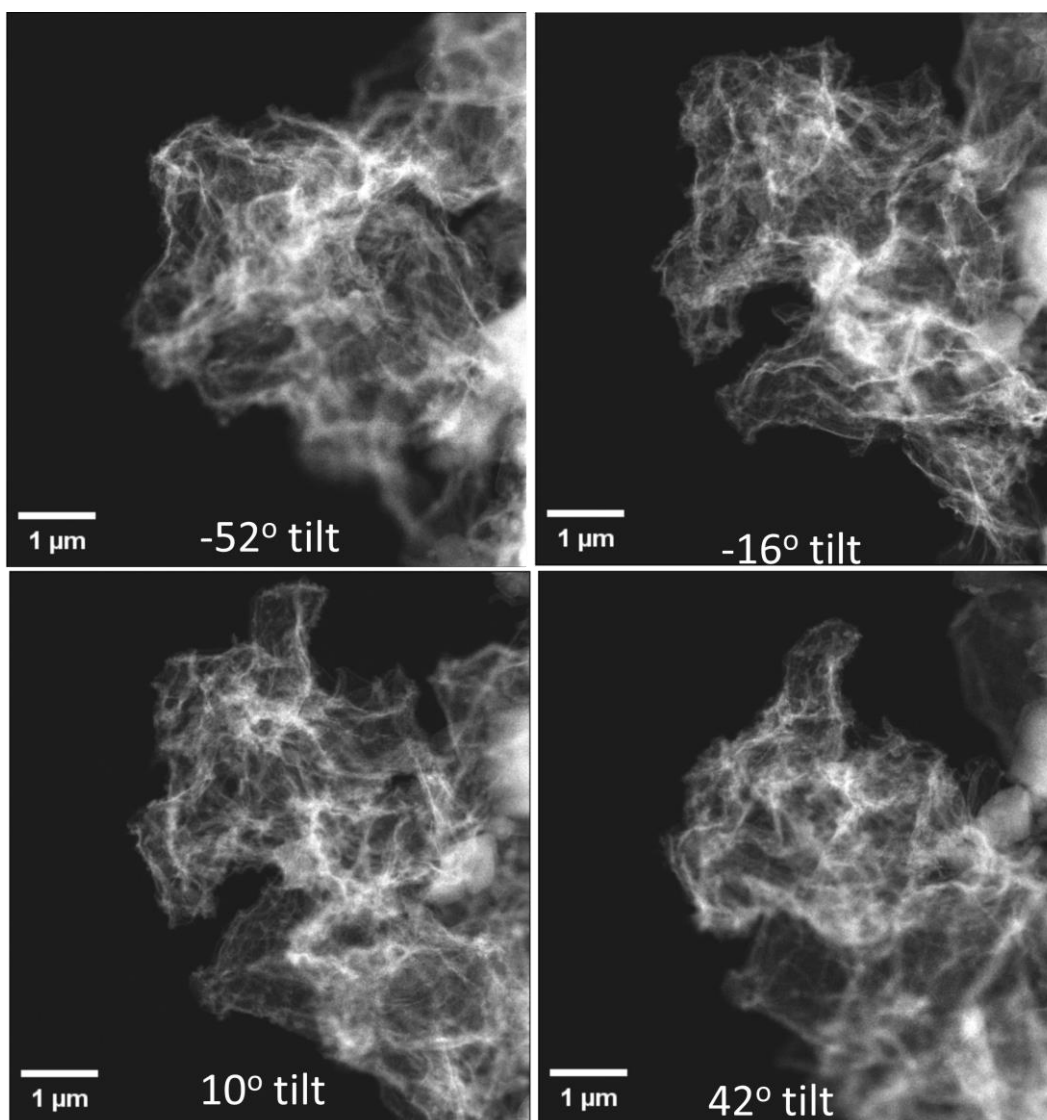
Figure S8. STEM tilt series of the SEI husk after 1st round of Li stripping using EC:DEC-FEC electrolyte with LiPF$_6$ salt, showing large size and porous structure. Please note that the two particle-shaped objects are ice particles from the sample preparation
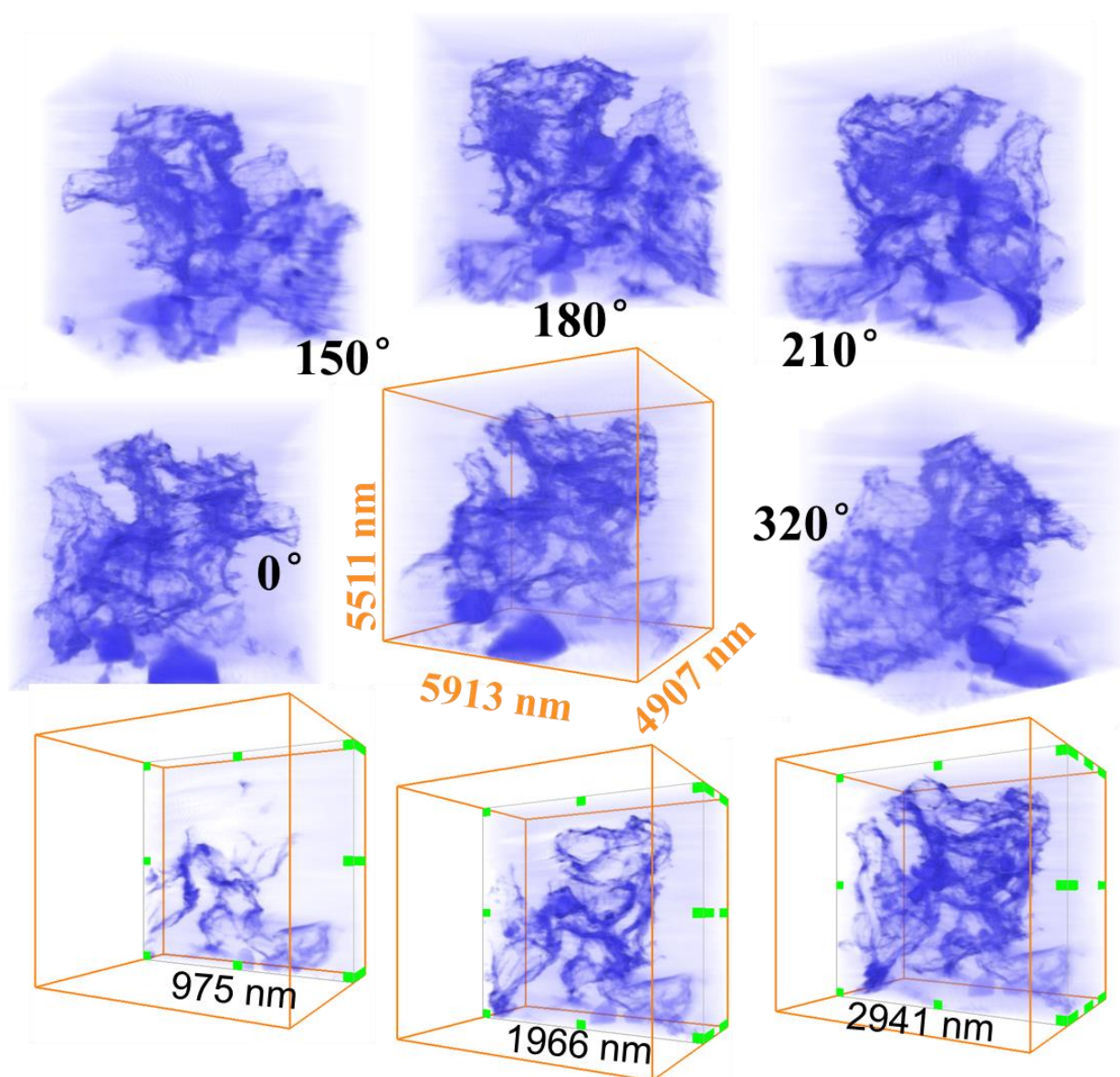
Figure S9. Comparative 3D tomography and cross-sectional slicing view of the porous SEI network after Li stripping in EC:DEC-FEC electrolyte with $LiPF_6$ (see also Movie S7-S9 to view the pores inside the SEI husk.
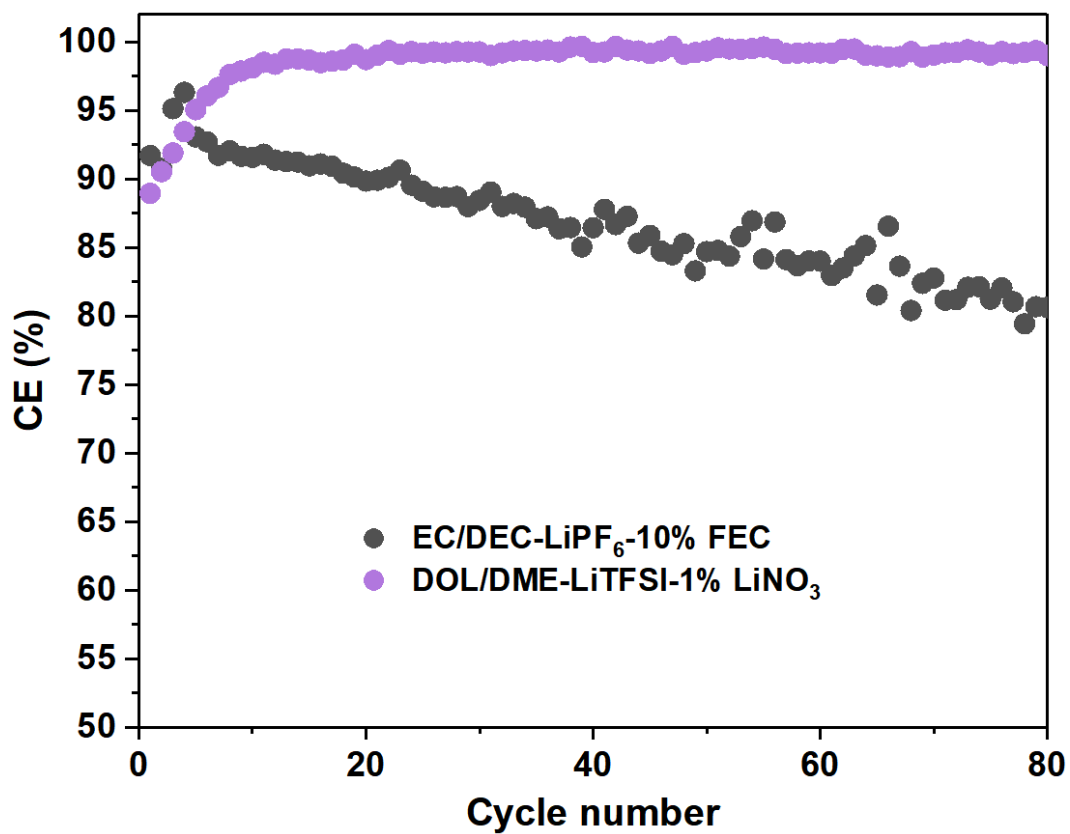
Figure S10. Comparison of the CE in carbonate-based EC/DEC-FEC electrolyte and ether-
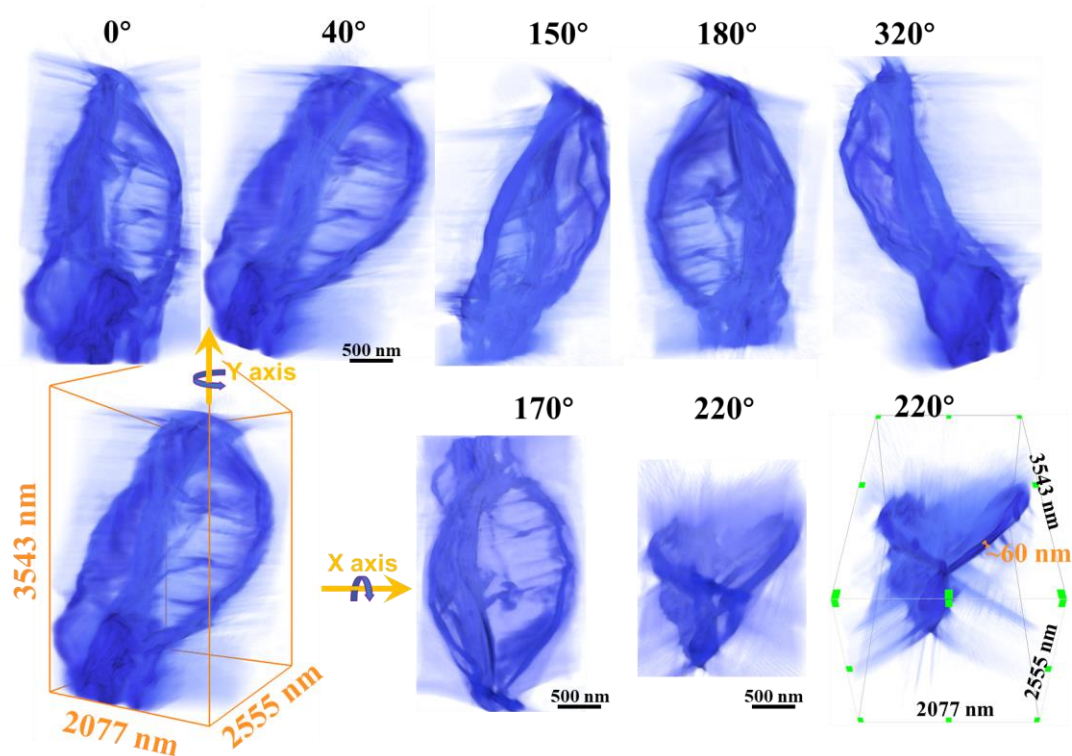
based DOLDME-LiTFSI electrolyte.

Figure S11. STEM tomography showing the Li-filled SEI husk at 2nd round of platting up to 0.1mAh/cm^2 energy capacity using DOLDME-LiTFSI with 1% LiNO$_3$. Please note that we rotated the particle along both Y and X axis to show ultra-thin layer of Li grown inside the SEI husk. Please see also Movie S11 & S12 for rotational view animations.
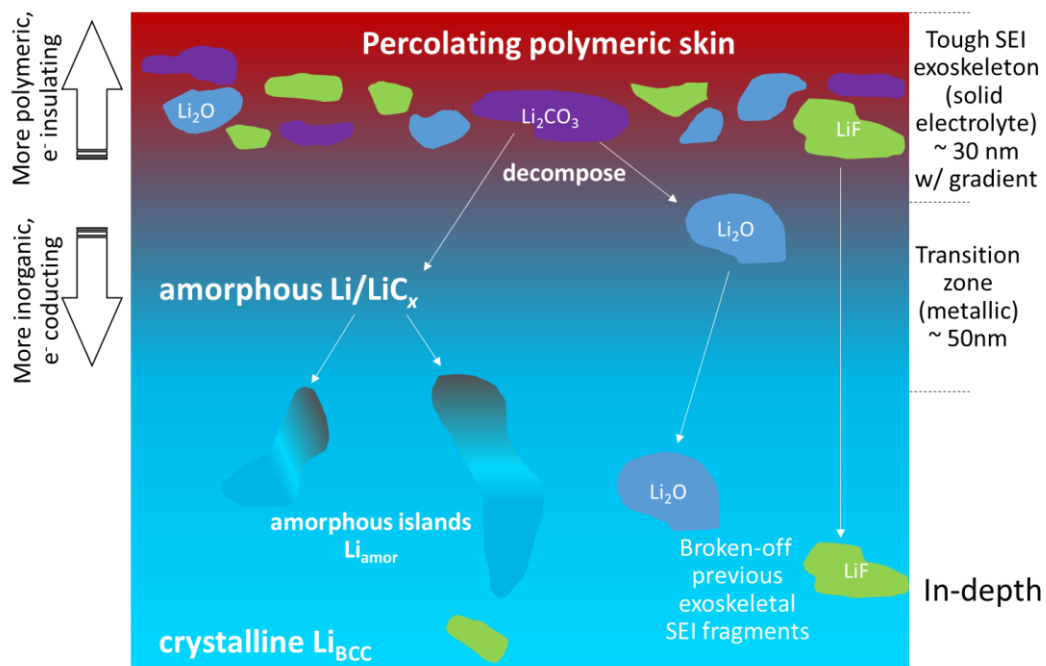
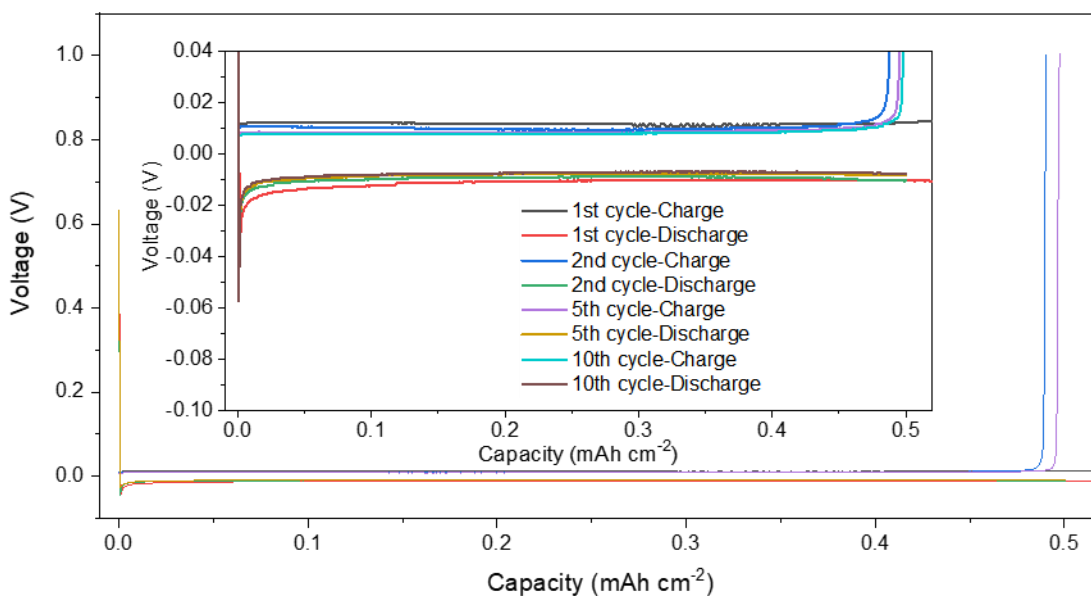**Figure S12.** SEI model based on our cryo-electron microscopy analysis

Figure S13. Electrochemical voltage curves showing near-zero overpotential on 2nd and

further cycles.

Table S1. The tilt angle range of reconstructed tomography.

reconstructed tomography	range of tilt angles
Figure 2H	$-46^o \sim +46^o$
Figure 3D	$-50^o \sim +50^o$
Figure 3J	$-66^o \sim +66^o$
Figure 4D/S5	$-50^o \sim +50^o$